# Molecular dynamics simulation of latent track formation in α-quartz[*]

LAN Chun-E(兰春娥)[1]    XUE Jian-Ming(薛建明)[1,2;1)]    WANG Yu-Gang(王宇钢)[1,2]
ZHANG Yan-Wen(张燕文)[3,4]

[1] State Key Laboratory of Nuclear Physics and Technology, School of Physics, Peking University, Beijing 100871, China
[2] Center for Applied Physics and Technology, Peking University, Beijing 100871, China
[3] Department of Materials Science & Engineering, University of Tennessee, Knoxville, TN 37996, USA
[4] Materials Science & Technology Division, Oak Ridge National Laboratory, Oak Ridge, TN 37831, USA

**Abstract:** The latent ion track in α-quartz is studied by molecular dynamics simulations. The latent track is created by depositing electron energies into a cylindrical region with a radius of 3 nm. In this study, the electron stopping power varies from 3.0 keV/nm to 12.0 keV/nm, and a continuous latent track is observed for all the simulated values of electron stopping power except 3.0 keV/nm. The simulation results indicate that the threshold electron stopping power for a continous latent track lies between 3.0 keV/nm and 3.7 keV/nm. In addition, the coordination defects produced in the latent track are analyzed for all the simulation conditions, and the results show that the latent track in α-quartz consists of an O-rich amorphous phase and Si-rich point defects. At the end of this paper, the influence of the energy deposition model on the latent track in α-quartz is investigated. The results indicate that different energy deposition models reveal similar latent track properties. However, the values of the threshold electron stopping power and the ion track radius are dependent on the choice of energy deposition model.

**Key words:** latent ion track, α-quartz, coordination defects, molecular dynamics simulation

**PACS:** 02.70.Ns, 31.15.xv    **DOI:** 10.1088/1674-1137/37/3/038201

## 1    Introduction

When energetic ions penetrate a solid material, they lose their energies through elastic collisions with target nuclei (nuclear stopping) and inelastic collisions with target electrons (electron stopping). For swift heavy ions with energy of MeV to GeV, the electron stopping dominates the energy loss processes and the contribution of nuclear stopping is negligible. The interactions of the incident ion with the target electrons excite the electrons in the solid materials. When the electron stopping power $((\mathrm{d}E/\mathrm{d}x))$ of the incident ion is higher than a material dependent value, namely the threshold electron stopping power $((\mathrm{d}E/\mathrm{d}x)_{\mathrm{th}})$, the electron excitations lead to a continuous cylindrical damaged zone, namely the ion track.

Theoretical descriptions of the latent ion track have been made for several decades. Among all the proposed models, the Coulomb explosion [1, 2] and the thermal spike model [3–5] are most widely discussed. Due to a lack of macroscopic material parameters when the lattice atoms are strongly ionized by the projectile, sufficiently

developed Coulomb explosion descriptions, which can correctly reproduce experimental observations or provide useful predictions, are still unavailable. On the other hand, the thermal spike model has been used to successfully describe the evolution of the experimental track radius with electron stopping for various metals and insulators [5–8]. However, due to a lack of information on the nonequilibrium thermodynamical property of the material, the applicability of the thermal spike concept is sometimes heavily disputed because of the use of equilibrium heat transport. In this case, computer simulation provides a direct way to gain an insight into the latent track formation.

The molecular dynamics (MD) method has been widely used in ion track simulations [9–18]. Most of the published literatures on ion track simulations use the homogenous energy depositions, and the temperature profiles are used as a tool to define the ion track radius. The simulation results for Ar ions indicate that the energy transportations described by the thermal spike model are not strictly correct [10, 11]. The temperature profiles for the Gaussian-distributed energy deposition and the

homogeneous deposition are the same after a few ps, which indicates that the energy deposition profiles have negligible effect in the MD simulations of ion track formation. By using an energy deposition profile calculated from the inelastic thermal spike model, a low-density core–high-density shell fine structure has been observed in various materials [12, 14, 15]. In addition, the authors pointed out that the results were somewhat dependent on the choice of the energy deposition model. Until now, the dependence of the ion track radii on the electron stopping power and the structure of the ion track in α-quartz were well studied [12, 14, 16]. However, none of the simulations provide insight into the defects produced in the latent track formation in α-quartz. The goal of this paper is to study the defects produced in the latent track formation in α-quartz and the influence of the energy deposition model on the track formation.

## 2    Simulation method

The simulations were performed with LAMMPS [19] and the trajectories were visualized with VMD [20]. The Watanabe potential for a Si-O mixed system [21, 22], which has been shown to be well suited to study the radiation defects in $SiO_2$ [12, 15, 23], was used to calculate the atomic interactions. The potential was smoothly joined to the universal Ziegler-Biersack-Littmark potential by the Fermi function at a close distance to avoid unphysical interactions. The α-quartz used in the simulations was 20.9 nm×21.2 nm×9.9 nm and contained 326592 atoms. Periodic boundary conditions were used in the three dimensions.

The α-quartz was initially equilibrated in the isothermal isobaric ensemble at 300 K and zero external pressure for 30 ps. A latent ion track was subsequently created along the z direction by depositing the electron energy simultaneously to a cylindrical region with a radius of 3 nm [13, 17, 18], and all the atoms in this region obtained the same amount of energy, with their initial velocities randomly distributed. The total deposited energy corresponds to the electron stopping power of the incident ion. In this study, the electron stopping power varied from 3.0 keV/nm to 12.0 keV/nm. The simulated electron stopping power and the corresponding deposited energy per atom in the deposition region are displayed in Table 1.

When the electron energy deposition was finished, the evolution of the sample was followed with the microcanonical (constant NVE) ensemble, during which the temperature of the last 0.5 nm at the borders in the $x$ and $y$ directions was controlled at 300 K by Berendsen method [24]. A variable time step from 0.01 ps to 0.1 ps was used. The simulations were terminated until the temperature of the sample was below 500 K, and no

change was observed in further simulations.

The defects of the irradiated sample were identified by the coordination number. A cutoff radius of 0.2 nm was used for the Si-O bond, i.e. only the Si(O) atoms that were within 0.2 nm of an O(Si) atom contribute to the coordination number of this O(Si) atom. An atom was identified to be a coordination defect if the coordination number of silicon was not equal to 4 or the coordination number of oxygen was not equal to 2. A coordination defect was identified to be part of an amorphous region if more than half of its neighbors were also coordination defects; otherwise it was identified to be a point defect.

Table 1.   The values of electron stopping power ($dE/dx$) in the present work and the corresponding energy that one atom in the energy deposition region obtains.

| $dE/dx$/(keV/nm) | energy per atom/(eV/atom) |
|---|---|
| 3.0 | 1.42 |
| 3.7 | 1.75 |
| 4.6 | 2.18 |
| 5.2 | 2.46 |
| 7.1 | 3.37 |
| 9.0 | 4.27 |
| 12.0 | 5.69 |

## 3    Results and discussion

### 3.1    The dependence of ion track radius on the electron stopping power

Figure 1 displays the evolution of the sample in the $x$-$y$ plane within 2 ps for $dE/dx$=12.0 keV/nm. The radial transportation of the energy in the latent track formation proceeds as follows. The initially excited atoms collide with their neighbors and after a few collisions, a fraction of the energy is transported away by the neighbors. In addition, a radial outgoing pressure wave is formed due to the physical expansion of the excited region. A rarefaction then occurs, associated with the density lowering in the center. The pressure wave slows down with time and the lattice atoms return to the center region. We believe that the entire scenario is a weak unsteady shock wave phenomenon [10]. After several ps the pressure wave diminishes and a stable continous amorphous phase forms.

The ion track radius is determined by visualizing the amorphous region in VMD as shown in Fig. 2. For $dE/dx$=3.0 keV/nm (shown in Fig. 2(a)), no obvious amorphous region can be seen, except for a few point defects. A continous cylindrical amorphous region, with an unclear boundary between the amorphous phase and the crystalline region, is observed when the electron stopping power increases to 3.7 keV/nm. The amorphous
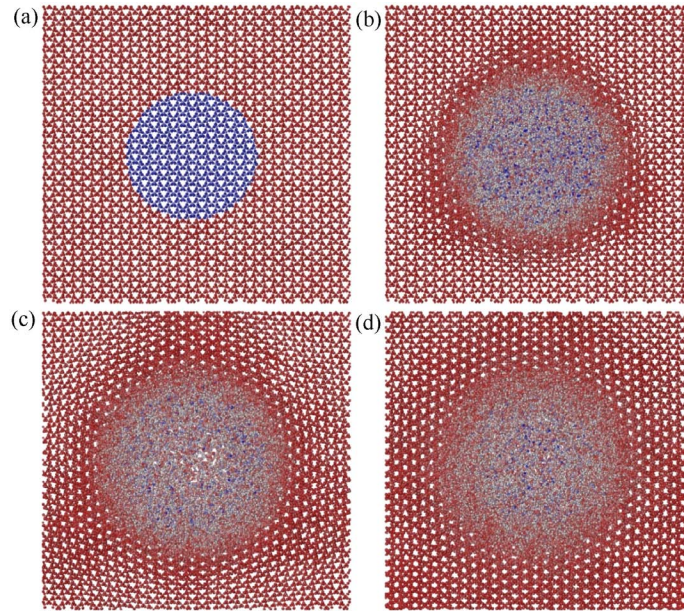
Fig. 1.    (color online) Sample evolutions in the $x$-$y$ plane with time within 2 ps for d$E$/d$x$= 12.0 keV/nm. Atoms are colored from red to blue to represent the kinetic energies from low to high.
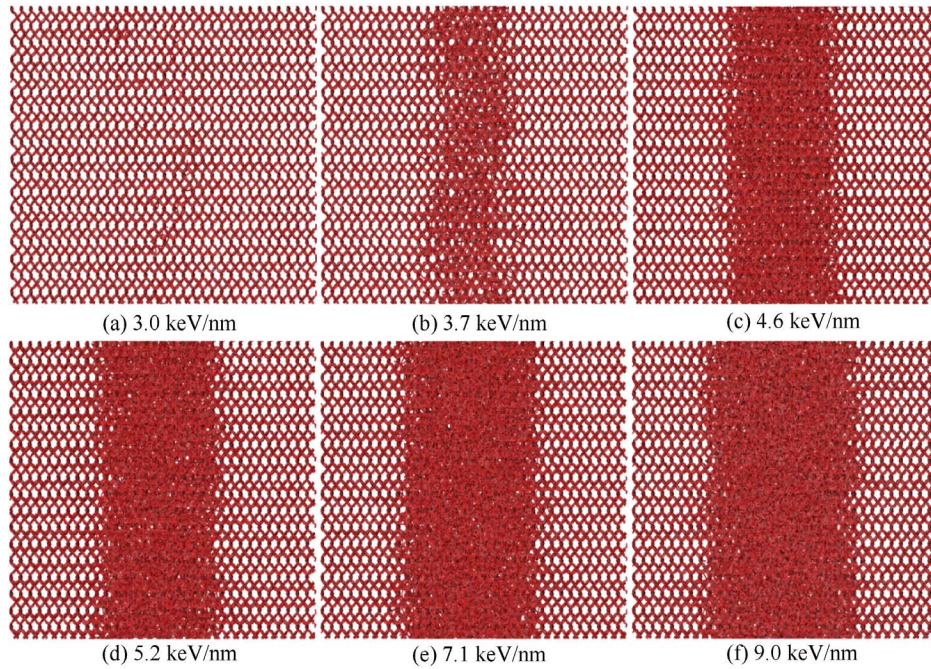


Fig. 2.    Final configurations of α-quartz along the $z$ direction (track axis) for different values of electron stopping power.

region expands and the boundary becomes more clear as the electron energy loss continues to increase. These results indicate that the minimum electron stopping power for continous track formation ($(\mathrm{d}E/\mathrm{d}x)_{\mathrm{th}}$) lies between 3.0 keV/nm and 3.7 keV/nm. This result is close to the previous simulated value of 3.6 keV/nm [12].

The simulated ion track radii for different values of electron stopping power are shown in Fig. 3. The experimental data and previous MD simulation results are also displayed for comparison [6, 12]. As can be seen from the figure, the ion track radius increases with increasing the electron stopping power. The simulated track radii are in overall good agreement with the experimental data and the previous simulation results, and the small diviations result from the homogenous energy deposition model used in the present study. In this deposition model, the ion track radius is only dependent on the electron stopping power, and the velocity effect,
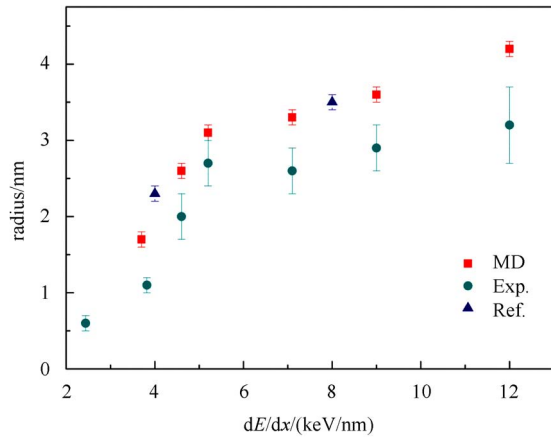
Fig. 3.   (color online) The latent ion track radius as a function of electron stopping power. Fig. 2. The simulation results in this study (diamond) are compared with the experimental data in Ref. [6] (circles) and the previous MD simulation results in Ref. [12] (triangles).

i.e. the damage cross section is higher at low ion velocity than that at high ion velocity for the same value of electron stopping power [6, 25], is neglected. Therefore, the

simulated track radius is deviated from the experimental data when the ion track radius is affected by the incident ion velocity greatly.

## 3.2   Coordination defect in the latent ion track

The coordination defects produced in the track formation were analyzed for all of the simulations. Fig. 4 and Fig. 5 show the point defect number and the defect number in the amorphous phase as a function of time for different values of electron stopping power, respectively. The results for the two lowest values of electron stopping power (3.0 keV/nm and 3.7 keV/nm) are separately plotted in Fig. 4(a) and Fig. 5(a) for clarity. As can be seen from Fig. 4, a similar trend for the point defect number with time was observed over a wide range of electron stopping power. Take $\mathrm{d}E/\mathrm{d}x$=12.0 keV/nm as an example: the point defect number increases quickly at the beginning, and reaches its peak of ~8000 at about 10 ps. Then this number decreases and becomes stable to ~3500 after 30 ps, indicating that the simulation time is long enough. The rise and fall of the curve correspond to the defect producing and defect annealing processes in the track formation, respectively, and more than half
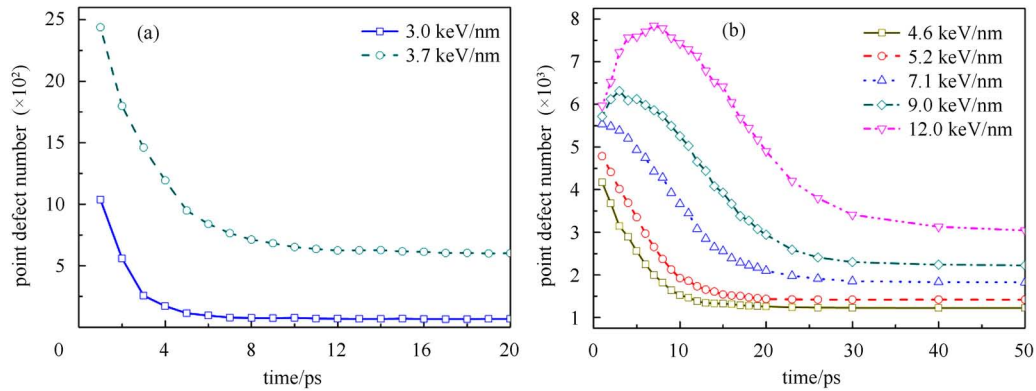


Fig. 4.   (color online) Evolution of the point defect number with time for different values of electron stopping power.
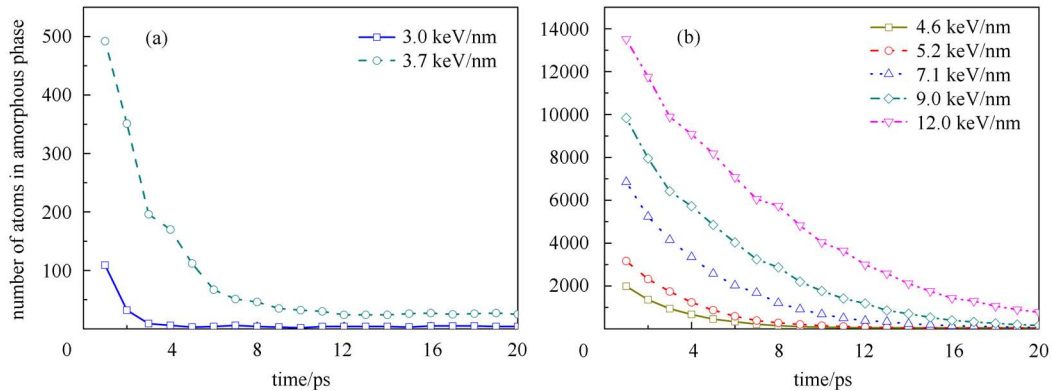


Fig. 5.   (color online) Evolution of the defect number in the amorphous phase with time for different values of electron stopping power.

of the point defects are recombined at the end of the simulation. For lower values of electron stopping power, the time for both defect producing and annealing processes is greatly shortened. Furthermore, the maximum and steady point defect number decrease with decreasing the value of electron stopping power. For $dE/dx$=3.0 keV/nm, the steady point defect number is less than 100.

As can be seen from Fig. 5, the evolutions of the defect number in the amorphous phase with time follows a similar trend as the point defects. For $dE/dx$=3.0 keV/nm, no steady amorphous phase is observed; indicating that there is no ion track at the end of the simulation. Both the maximum and steady defect number in the amorphous region increase with increasing the electron stopping power. These results are consistent with the dependence of the ion track radius on the electron stopping power, as shown in Fig. 3.

In order to have a better sense of the defects in the latent track, the chemical compositions of both the point defects and the defects in the amorphous phase at the end of the simulations were analyzed and the results are shown in Fig. 6. In α-quartz, the number of O atoms is twice the number of Si atoms. If the defects are produced stoichiometricly, the number of O defects should also be twice the number of Si defects. However, as can be seen from Fig. 6(a), the number of O point defects is much less than twice the number of Si point defects. This non-stoichiometric point defect production may be due to the different threshold displacement energies of O and Si. On the other hand, Fig. 6(b) shows that the amount of O in the amorphous phase is more than twice the amount of Si. This may be related to the different recovery schemes for O recoils and Si recoils. The previous simulations show that in amorphous silica, silicon recoils have a higher flexibility for defect recombination than oxygen recoils in producing a stable oxygen vacancy [26]. These results indicate a structure with a O-rich amorphous phase with Si-rich point defects of the latent ion track in α-quartz.

## 3.3 Influence of the energy deposition model on the latent track

In this paper, a simple homogenous energy deposition model was used; although it is widely used in ion track simulations, it is not physically correct as it neglects the radial distributions of the deposited energy and the velocity effect [25]. In order to investigate the influence of the energy deposition model on the latent ion track, an inhomogeneous energy deposition model, in which the energy deposition is dependent on the velocity and effective charge of the incident ion, was also applied [27]. Other simulation conditions were the same as previously described.
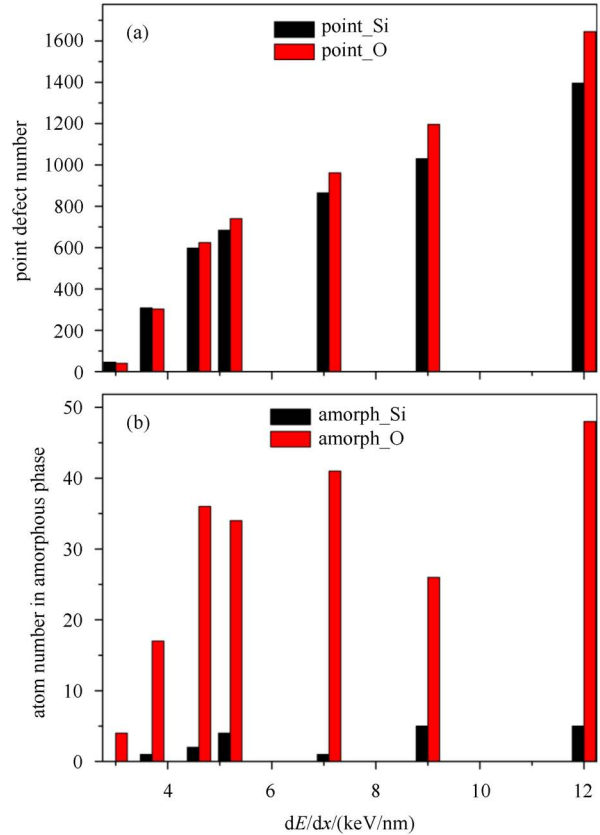


Fig. 6. (color online) The number of Si and O (a) point defects and (b) in amorphous phase for different values of electron stopping power.

Figure 7 shows the sample evolution in the $x$-$y$ plane for the inhomogeneous energy deposition model with $dE/dx$=2.5 keV/nm. Seen from the figure, only a small region of atoms in the center is initially of high kinetic energy. However, the pressure wave phenomenon mentioned above was also observed, and an O-rich amorphous region and a Si-rich defect structure were found. These results indicate that the latent ion track features in α-quartz are independent of the choice of energy deposition model.

The values of $(dE/dx)_{\rm th}$ for different energy deposition models were explored. For the homogenous energy deposition model applied above, the deposition radius was changed to 2.5 nm and 2 nm to explore the influence of the energy deposition radius on the $(dE/dx)_{\rm th}$. The simulation results show that the value of $(dE/dx)_{\rm th}$ decreases with decreasing the energy deposition radius. The $(dE/dx)_{\rm th}$ lies between 2.0 keV/nm and 2.5 keV/nm when the deposition radius is 2.5 nm, and the $(dE/dx)_{\rm th}$ lies between 1.5 keV/nm and 2.0 keV/nm when the deposition radius changes to 2.0 nm. This is attributed to the same amount of total deposited energy in the sample. For the same value of electron stopping power, a larger energy deposition radius results in a larger energy dep-
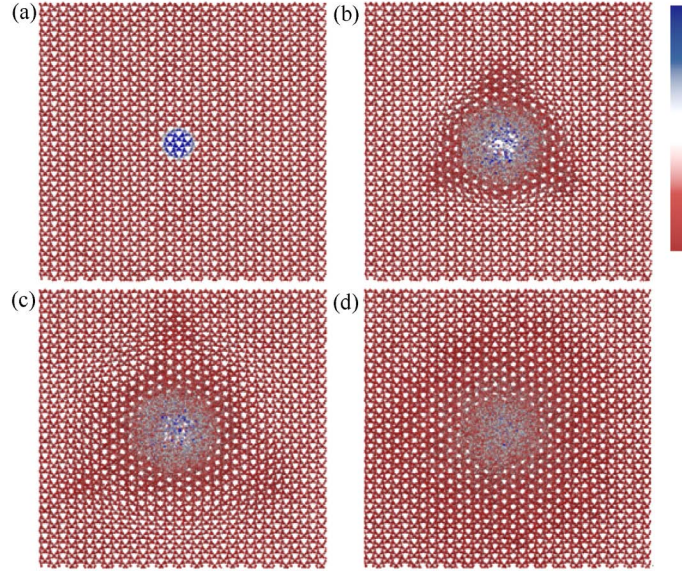
Fig. 7.  (color online) Sample evolutions in the $x$-$y$ plane with time within 2 ps for the inhomogeneous energy deposition model with $dE/dx$=2.5 keV/nm. Atoms are colored from red to blue to represent the kinetic energies from low to high.

osition region, and correspondingly, the kinetic energy that each atom obtains decreases and fewer atoms have enough energy for melting.

The $(dE/dx)_{th}$ for the inhomogeneous energy deposition model lies between 1.5 keV/nm and 2.0 keV/nm, which is similar to that for the homogenous energy deposition model with a deposition radius of 2.0 nm. However, for the same irradiation condition, different values of ion track radius may be obtained from these two models. For the homogenous deposition model, the deposition region and the kinetic energy that one atom obtains are only dependent on the electron stopping power. So any ion with the same value of electron stopping power would induce the same ion track radius. On the other hand, for the inhomogeneous energy deposition model, the energy deposition is influenced by the type and velocity of the incident ion. As a result, different ions with the same electron stopping power may lead to different ion track radii.

From the above discussions, it seems that the inhomogeneous energy deposition model is more suitable to describe the ion track formation. However, the deposition formula was used to describe the energy deposited into the electron subsystem from the incident ion, and the efficiency of the energy deposition from the electron subsystem to the lattice subsystem is still unclear. On one hand, part of the energy would be lost during the electron-phonon coupling process. On the other hand, according to the equipartition of the energy, half of the kinetic energy would be immediately converted into the potential energy, so twice of the kinetic energy should be deposited. Considering these uncertainties, we chose to report the energy deposition model in our simulations, which is simple enough and also reveals proper features of the latent track in $\alpha$-quartz.

## 4    Conclusion

In this paper, the ion track formation in $\alpha$-quartz was investigated by molecular dynamics simulations. The ion track was created by simultaneously depositing the electron energies into a cylindrical region with a radius of 3 nm, and the simulation results indicate that the $(dE/dx)_{th}$ lies between 3.0 keV/nm and 3.7 keV/nm. Higher values of electron stopping power induce larger ion track radius. The dependence of the ion track radius on the electron stopping power is in good agreement with previous publications. In addition, the coordination defects produced in the ion track were analyzed. The results show that the ion track in $\alpha$-quartz consists of an O-rich amorphous region and Si-rich point defects.

The dependence of the track formation on the energy deposition model was also explored. Similar features were observed for two different energy deposition models. However, the threshold electron stopping power and the ion track radius are different for different energy deposition methods. For the homogenous energy deposition model, $(dE/dx)_{th}$ increases with increasing the energy deposition radius. The value of $(dE/dx)_{th}$ for the inhomogeneous energy deposition model is similar to that for the homogenous energy deposition model with a deposition radius of 2.0 nm. More theoretical efforts need to be done to define a more physical meaningful energy deposition model.

# References

1  Fleische R L, Price P B, Walker R M. J. Appl. Phys., 1965, **36**: 3645–3652
2  Lesueur D, Dunlop A. Radiat. Eff. Defects. S, 1993, **126**: 163–172
3  WANG Z G, Dufour C, Paumier E et al. J. Phys-Condens. Mat., 1994, **6**: 6733–6750
4  Volkov A E, Borodin V A. Nucl. Instrum. Methods B, 1998, **146**: 137–141
5  Toulemonde M, Dufour C, Meftah A et al. Nucl. Instrum. Methods B, 2000, **166**: 903–912
6  Meftah A, Brisard F, Costantini J M et al. Phys. Rev. B: Condens. Matter, 1994, **49**: 12457–12463
7  Toulemonde M, Constantini J M, Dufour C et al. Nucl. Instrum. Methods B, 1996, **116**: 37–42
8  Toulemonde M, Assmann W, Dufour C et al. Ion Beam Science: Solved and Unsolved Problems, Pts 1 and 2, 2006, **52**: 263–292
9  Abromeit C, Kuznetsov A R. Nucl. Instrum. Methods B, 2004, **225**: 97–104
10  Bringa E M, Johnson R E. Nucl. Instrum. Methods B, 1998, **143**: 513–535
11  Bringa E M, Johnson R E, Dutkiewicz L. Nucl. Instrum. Methods B, 1999, **152**: 267–290
12  Kluth P, Schnohr C S, Pakarinen O H et al. Phys. Rev. Lett., 2008, **101**: 175503
13  Moreira P A F P, Devanathan R, Weber W J. J. Phys-Condens. Mat., 2010, **22**: 395008
14  Pakarinen O H, Djurabekova F, Nordlund K. Nucl. Instrum. Methods B, 2010, **268**: 3163–3166
15  Pakarinen O H, Djurabekova F, Nordlund K et al. Nucl. Instrum. Methods B, 2009, **267**: 1456–1459
16  Phillips C L, Magyar R J, Crozier P S. J. Chem. Phys., 2010, **133**: 144711
17  Schwen D, Bringa E M. Nucl. Instrum. Methods B, 2007, **256**: 187–192
18  ZHANG J M, LANG M, Ewing R C et al. J. Mater. Res., 2010, **25**: 1344–1351
19  Plimpton S. J. Comput. Phys., 1995, **117**: 1–19
20  Humphrey W, Dalke A, Schulten K. J. Mol. Graph. Model., 1996, **14**: 33–38
21  Watanabe T, Fujiwara H, Noguchi H et al. Jpn. J. Appl. Phys., Part 2-Letters, 1999, **38**: L366–L369
22  Watanabe T, Yamasaki D, Tatsumura K et al. Appl. Surf. Sci., 2004, **234**: 207–213
23  Ohta H, Hamaguchi S. J. Vac. Sci. Technol. A, 2001, **19**: 2373–2381
24  Berendsen H J C, Postma J P M, Vangunsteren W F et al. J. Chem. Phys., 1984, **81**: 3684–3690
25  Szenes G. Phys. Rev. B: Condens. Matter, 1995, **52**: 6154–6157
26  Mota F, Caturla M J, Perlado J M et al. Fusion. Eng. Des., 2005, **75-79:** 1027–1030
27  Waligorski M P R, Hamm R N, Katz R. Nucl. Tracks. Rad. Meas., 1986, **11**: 309–319